Introduction of a nitrate anion with solubility mediator in a carbonate-based electrolyte for a stable potassium metal anode

Energy Storage Materials 69 (2024) 103443

Contents lists available at ScienceDirect

Energy Storage Materials

journal homepage: www.elsevier.com/locate/ensm

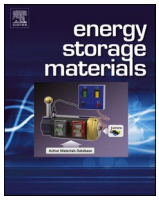

Introduction of a nitrate anion with solubility mediator in a carbonate-based electrolyte for a stable potassium metal anode

Jimin Park [a], Hyokyeong Kang [a], Marco Agostini [b,c,*], Shizhao Xiong [d], Shivam Kansara [a], Xieyu Xu [e], Yangyang Liu [e], Jang–Yeon Hwang [a,f,**]

[a] Department of Energy Engineering, Hanyang University, Seoul 04763, Republic of Korea
[b] Department of Chemistry and Drug Technologies, Sapienza University of Rome, P.le Aldo Moro 5, Rome 00185, Italy
[c] Department of Physics, Chalmers University of Technology, Göteborg SE 412 96, Sweden
[d] Faculty of Materials Science and Engineering, Kunming University of Science and Technology, Kunming 650093, China
[e] State Key Laboratory for Mechanical Behavior of Materials, Xi'an Jiaotong University, 28 Xianning West Road, Xi'an, Shaanxi 710049, China
[f] Department of Battery Engineering, Hanyang University, Seoul 04763, Republic of Korea

ARTICLE INFO

Keywords:
K-metal anodes
Dendrite
Solid electrolyte interphase layer
$NaNO_3$ additive
Phase-field modelling

ABSTRACT

In this study, sodium nitrate ($NaNO_3$) dissolves in a carbonate electrolyte for K-metal batteries (KMBs) using a dimethylacetamide (DMA) solvent with a higher Gutmann donor number than that of NO_3^-. The K-metal anode in 0.02 M $NaNO_3$ electrolyte exhibits enhanced stability due to the modified solid-electrolyte interphase (SEI) layer resulting from the preferential reduction of $NaNO_3$. Reduced $NaNO_3$ forms ionically conductive and mechanically robust compounds in the SEI layer. This compound plays a critical role in altering the morphology of electrodeposited K-metal from dendritic to spherical, reducing the barrier energy of nucleation potential for K-ions. These unique features make K-metal highly resistant to dendrite formation and aggressive electrolyte chemistry. Therefore, the K-metal anode in the proposed electrolyte containing 0.02 M $NaNO_3$ additive ensures excellent cycle life with stable Coulombic efficiency in both symmetrical K/K half cells and full-cells coupled with a Prussian green $FeFe(CN)_6$ cathode.

1. Introduction

Rechargeable potassium batteries offer sustainable alternatives to lithium-ion batteries (LIBs), that could allow for large-scale energy storage. This potential arises from several key advantages, such as K's low reduction potential compared to that of Li (Li: -3.04 V / K: -2.93 V vs. the standard hydrogen electrode, SHE), its abundant availability of K within the crust of the Earth (Li: 0.0017 wt.%; / K: 2.36 wt.%), and its cost-effective nature [1–3]. K-ion batteries (KIBs) share chemical characteristics with rechargeable LIBs [2,4]. Graphite, a common anode for KIB, exhibits limited capacity (279 mAh g^{-1}), making it insufficient for high energy density requirements [5]. In contrast, utilizing K-metal as an anode proves advantageous, meeting the high demand for high energy density with its remarkable capacity (687 mAh g^{-1}) and low redox potential [2,3]. The practical use of K-metal in batteries faces challenges due to its high reactivity, leading to the degradation of organic carbonate solvents. This results in an uncontrolled interfacial reaction between electrolytes of K-metal, forming an unstable solid-electrolyte interphase (SEI) layer. Uneven deposition of K-ions on the K-metal anode accelerates dendritic K growth, causing short-circuit problems and separator penetration issues [2,3]. Extensive efforts have been made to address these challenges and focus on strategies such as (1) electrolyte modification [6–15], (2) the construction of host structures [16,17], and (3) the design of artificial SEI film [18,19]. These strategies were aimed at protecting the K-metal surface. Among these, electrolyte modification utilizing functional additives is a commonly employed strategy [6,10,14].

Lithium nitrate ($LiNO_3$) is a well-known additive controlling Li deposition [20–27]. NO_3^- can alter the morphology of deposited Li and the chemical properties of the SEI layer [20,22,26]. Liu et al. reported that an electrolyte with $LiNO_3$ additive (particularly the presence of NO_3^-) can alter the electrodeposit morphology of Li-metal from fibrous to spherical morphology during the plating process [20]. Additionally, inorganic Li_3N compounds from $LiNO_3$ reduction improve SEI layer

* Corresponding author at: Department of Chemistry and Drug Technologies, Sapienza University of Rome, P.le Aldo Moro 5, Rome 00185, Italy.
** Corresponding author at: Department of Energy Engineering, Hanyang University, Seoul 04763, Republic of Korea.
E-mail addresses: marco.agostini@uniroma1.it (M. Agostini), shizhao.xiong@kust.edu.cn (S. Xiong), jangyeonhw@hanyang.ac.kr (J. Hwang).

https://doi.org/10.1016/j.ensm.2024.103443
Received 26 February 2024; Received in revised form 24 April 2024; Accepted 30 April 2024
Available online 1 May 2024

elasticity and rigidity due to high ionic conductivity and mechanical properties [20,22]. The positive effects of $LiNO_3$ in lithium-metal batteries (LIBs) have prompted research exploring the usage of nitrate additives to stabilize K-metal anodes. Wang et al. used potassium nitrate (KNO_3) as an electrolyte additive for K-metal batteries (KMBs) [3]. They dissolved the KNO_3 in ether-based electrolyte solvent. Reduction of KNO_3 produced nitrogen and fluorine-rich compounds in the SEI layer, facilitating dense and uniform K-metal deposition under high current densities. However, due to their low oxidation stability, ether-based electrolytes are generally difficult to couple with high-voltage cathode materials. Therefore, exploring methods to dissolve nitrate additives in carbonate electrolytes with high oxidation stability could enhance the energy density of KMBs.

In this study, we propose an innovative strategy by introducing sodium nitrate ($NaNO_3$) as an additive to carbonate-based electrolytes for high-performance KMBs. We found that 0.02 M $NaNO_3$ can be dissolved in 0.5 M potassium hexafluorophosphate (KPF_6) in ethylene carbonate (EC):diethyl carbonate (DEC) (1:1, vol.%) electrolyte with a small amount of high donor dimethylacetamide (DMA) solvent as a dissolution mediator. Due to the preferential reduction of $NaNO_3$, ionically conductive and mechanically robust compounds are formed in the SEI layer [14,28,29]. Remarkably, the introduction of NO_3^- significantly alters the morphology of deposited K from dendritic fibers to spherical particles. This reduces nucleation potential, enabling dense and uniform deposition of K-metal [14,28]. Even under high capacity loading and current density, the proposed electrolyte substantially extends the lifetime of a K/K symmetric cell to over 1,000 h. Moreover, it facilitates K-metal full battery coupling with a low-cost Prussian green $FeFe(CN)_6$ cathode for more than 600 cycles.

2. Results and discussion

Three high Gutmann donor number (DN) solvents, namely gamma-butyrolactone (GBL), dimethyl sulfoxide (DMSO), and DMA, commonly used in alkali metal batteries, were chosen to facilitate the dissolution of the $NaNO_3$ additive in EC:DEC (1:1, vol.%). This selection was based on the strong Lewis basicity of high DN solvents to promote dissolution of $NaNO_3$ that possesses low dissociation energy to Na^+-NO_3^- in EC:DEC solvent [30,31]. Fig. 1a orders the solvents (EC:DEC, GBL, DMA, and DMSO) and NO_3^- by DN. Both DMA and DMSO solvents exhibited higher DN than NO_3^- and exhibited good dissolution capability in 0.5 M $NaNO_3$ (Fig. 1b) [32–35]. Despite their high DN, these solvents (strong Lewis basicity) generally exhibit strong reactivity against K-metal anode (strong Lewis acidity) [36]. Fig. S1 illustrates the oxidation of the K-metal surface and turned blue upon contact with the DMA, while DMSO triggers an explosive chemical reaction within a few seconds. Due to its mild reactivity (even with high DN), DMA was selected as a mediator solvent for $NaNO_3$ dissolution in a carbonate-based electrolyte solution. In this study, 0.5 M KPF_6 in EC:DEC (1:1, vol.%) electrolyte was served as baseline electrolyte (BE). To modify BE, DMA was introduced into BE (BE:DMA = 38.5:1, w/w.%) (D-BE). $NaNO_3$ was then added into D-BE by varying mole fractions of 0.02, 0.04, and 0.06 mol (denoted as D-2NE, D-4NE, and D-6NE, respectively) (Fig. 1c). To confirm the stability of interface between K-metal and EC/DEC with DMA electrolyte, we further checked chemical reactivity test of potassium metal with electrolytes using BE, D-2NE, and D-BE in Fig. S2a. K-metal surface in D-2NE and D-BE is not oxidized even after 20 h of contact. It was visually observed that the addition of a very small amount of DMA solvent into electrolyte did not affect the reactivity of potassium metal. This is also consistent with results of

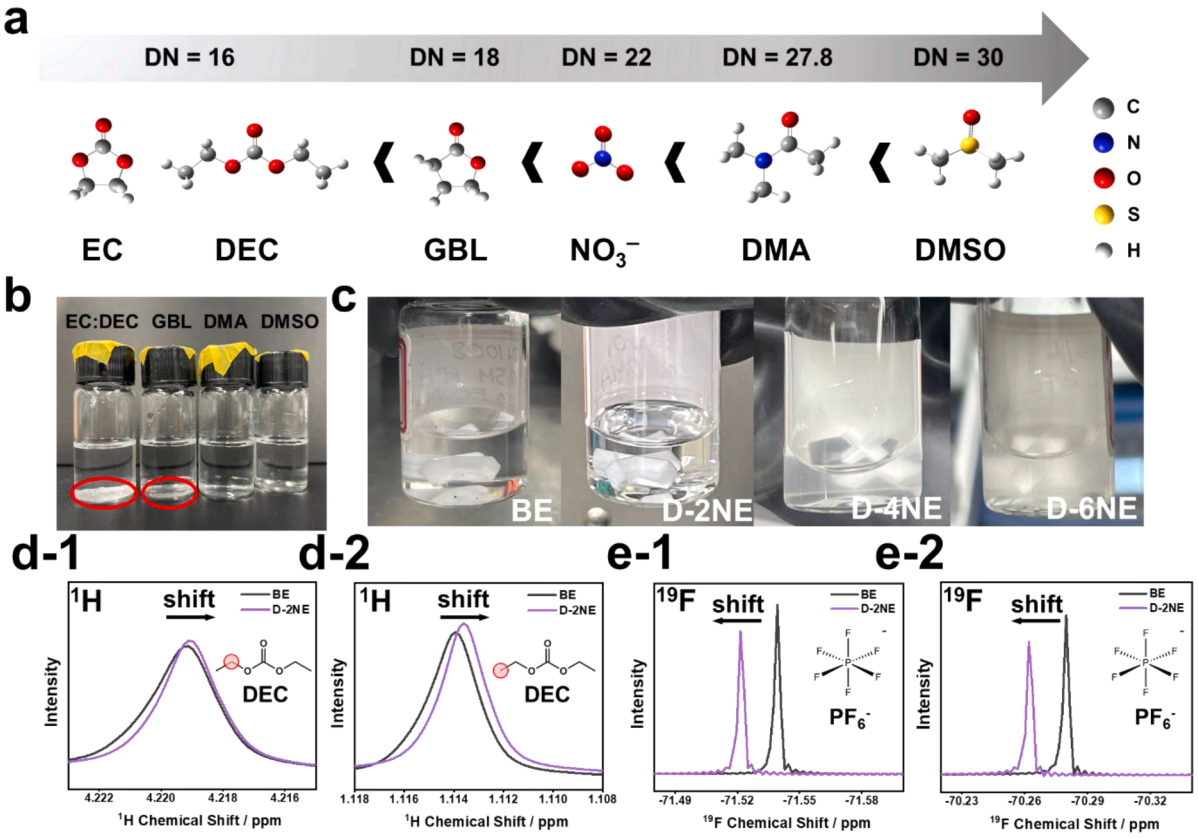

Fig. 1. (a) Donor number of solvents (EC, DEC, GBL, DMA, and DMSO) and NO_3^-. (b) Digital photographs of electrolyte supplemented with 0.5 M $NaNO_3$ electrolytes corresponding to different solvents (EC:DEC [1:1, vol.%], GBL, DMA, and DMSO). (c) Optical images of electrolytes corresponding to BE, D-2NE, D-4NE, and D-6NE. NMR spectra (600 MHz, 298 K) of (a) ^1H and (b) ^{19}F in electrolytes corresponding to BE and D-2NE; (d-1) CH_2 signal, (d-2) CH_3 signal, (e) PF signal. The position of H in the DEC molecule marked with red circle in ^1H NMR spectra.

self-discharge test during in the same range of time in Fig. S2b. Rather, the decomposition of the $NaNO_3$ additive (~1.6 V) with the low LUMO energy level results in forming a stable SEI layer and suppressing the degree of irreversible electrolyte decomposition assigned to carbonate reduction (Fig. S2c) [28]. Starting from D-4NE, the electrolyte became cloudy, and at D-6NE, the salt remained undissolved in the solution. This is important discovery, as the low solubility issue of nitrate additive in carbonate-based electrolyte solution can be resolved by the new approach of dissolving 0.02 mole of $NaNO_3$ into the D-BE. The dissolution of $NaNO_3$ in the D-BE was confirmed by nuclear magnetic resonance (NMR) spectroscopy (Fig. 1d and e). The ^{1}H spectrum exhibited up-field shifts associated with the chemical reaction between $NaNO_3$ and the EC/DEC solvents, indicating chemical shifts in the right direction upon adding $NaNO_3$ [37–39]. This is due to the observation that when the $NaNO_3$ additive was dissolved in D-BE, electron-rich (high DN) NO_3^- attracted the electron-deficient CH_2 group in EC and/or DEC molecule [40–42]. Conversely, the ^{19}F spectra show a down-field shift when $NaNO_3$ is added to D-BE, and this is attributed to the formation K^+-NO_3^- and K^+-DMA bonds that occur due to weakening of the K^+-PF_6^- bond [43–45]. Note that the displacement of PF_6^- from the cationic center in the solvation shell due to the weak K^+-PF_6^- bond can contribute to form a relatively large fraction of F-rich inorganic compound in the SEI layer. Along with NMR data, we predicted the potential solvation structure through the binding energy with K^+ through the DFT calculations (Fig. S3) [46–48]. EC, DEC, DMA and PF_6^- showed similar values, but NO_3^- had a much higher binding energy with K^+. The strong binding energy value between K^+ and NO_3^- suggested that NO_3^- can occupy the inner layer of the K^+ solvated structure in D-2NE [47,48].

To compare the 1st electrodeposition behavior of K-metal between BE and D-2NE, asymmetric K/Cu cells were fabricated. In these cells, K deposition onto a Cu substrate was conducted at a capacity loading of 1 mAh cm^{-2} and current density of 1 mA cm^{-2}. The morphologies were subsequently observed using scanning electron microscopy and corresponding elemental dispersive x-ray (EDX) analysis (Fig. 2a–d). In the case of BE, K-metal appeared to be loosely packed and possess an uneven island-type electrodeposit morphology on the Cu substrate. By contrast, D-2NE exhibited densely packed electrodeposit K-metal film on the Cu substrate. The K-metal completely covered the Cu substrate, D-2NE. Strikingly, spherical K-metal particles were observed in the presence of a $NaNO_3$ additive in the carbonate-based electrolyte, and this is generally attributed to the effect of NO_3^- [20,49,50]. Along with altering the solvation structure, the presence of NO_3^- drives the frontier reaction during SEI formation, such as the formation of an ionically conductive Na_3N compound (see the elemental mapping of the nitrogen atom) and plays an important role in changing the chemical properties of the SEI. During the 1st plating reaction in the K/Cu cells (Fig. 2e), D-2NE (0.209 V) exhibited a lower nucleation potential than that of BE (0.250 V) [51]. These features are also closely related to the exchange current density on the electrode surface [52]. The exchange current density is a crucial parameter reflecting the electrochemical kinetics of the plating process

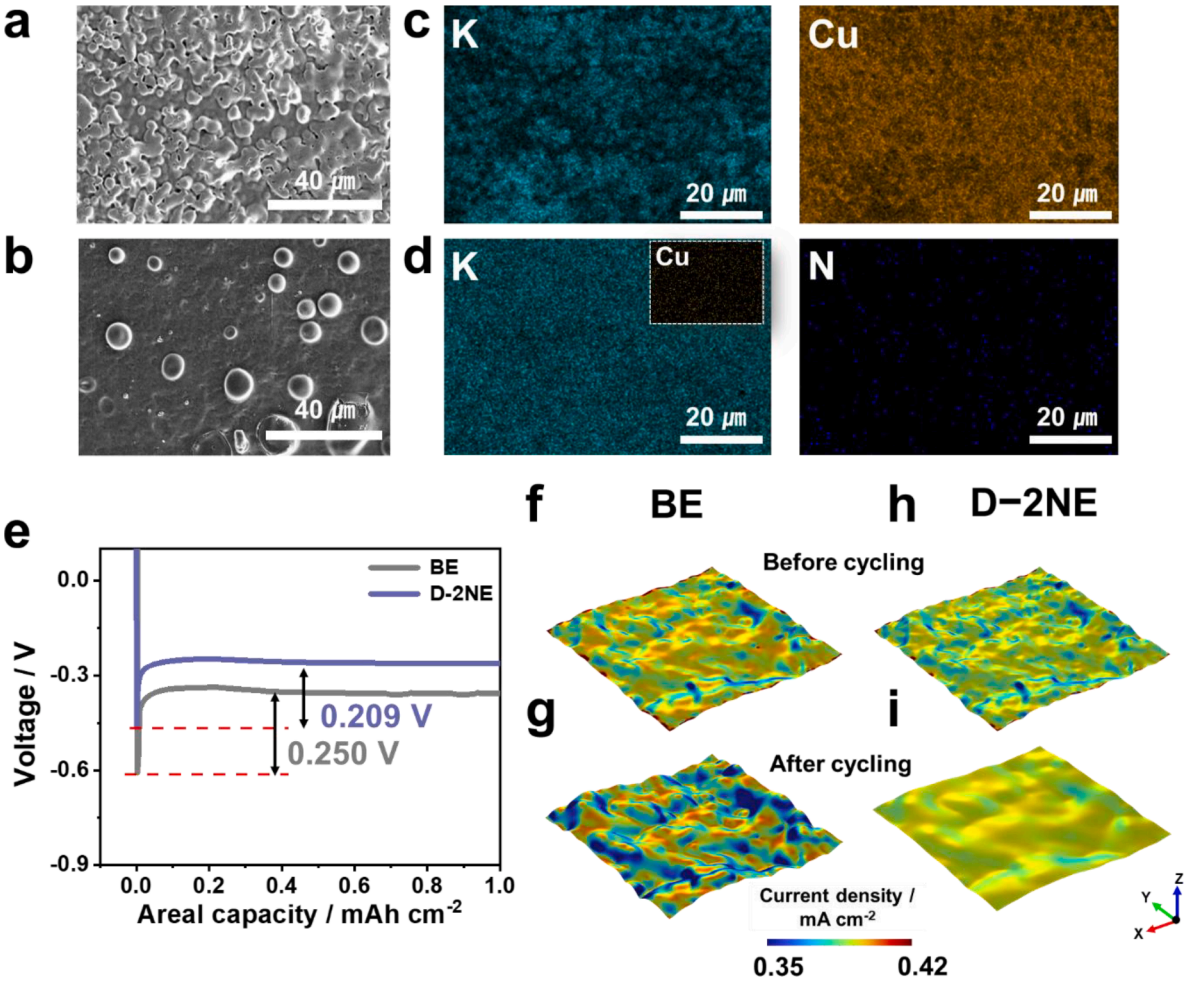

Fig. 2. SEM and EDX (K, Cu, and N) images corresponding to electrochemical K deposition on a Cu foil in different electrolytes at a current density of 0.4 mA cm^{-2} and capacity loading of 4 mAh cm^{-2} with (a and c) BE and (b and d) D-2NE. (e) Nucleation potential of the electrodeposited K in electrolytes with/without $NaNO_3$ additive at a current density of 0.1 mA cm^{-2} and capacity loading of 1 mAh cm^{-2}. Distribution of current densities on the substrate with (f and g) BE and (h and i) D-2NE (f and h) before and (g and i) after cycling.

and can be obtained from the Tafel plot based on linear sweep voltammetry (scan rate: 1 mV/s) (Fig. S5). Fig. S5 illustrates that the exchange current density of the D-2NE (1.97 μA) is ten-fold lower than that of the BE (19.95 μA). Previous studies suggest that the nucleation of K with a lower local current density results in larger nuclei for K deposition, thus leading to a uniform distribution of K^+ during electrodeposition, as indicated by phase-field modelling [53]. Therefore, the anticipated effects of the lower exchange current density and the spherical morphology of deposited K were to impede the growth of K seeds during electrodeposition and facilitate a uniform distribution of K^+. Tafel curves demonstrate that the introduction of $NaNO_3$ as an additive significantly reduces the exchange current density, suggesting the potential for uniform electrodeposition of K-metal with $NaNO_3$. To gain further insight into the behavior of K-metal growth during cycling, the morphology of K electrodeposition on the substrate with different electrolytes was visualized through multi-physical simulation. Initially, a 3D surface with random fluctuations was generated using a random function with roughness R_a=7.2 μm (Fig. S6). The exchange current density values for BE were set at 19.95 μA cm^{-2}, and for the D-2NE electrolyte they were set at 1.97 μA cm^{-2} and incorporated into the Butler-Volmer equation [53,54]:

$$J = j_0\left[\exp\left(\frac{\alpha F}{RT}\eta_c\right) - \exp\left(-\frac{(1-\alpha)F}{RT}\eta_a\right)\right] \quad (1)$$

including Faradic current density (J), the exchange current density (j_0), the overpotential (η), the molar gas constant (R), the temperature (T), and the anodic charge-transfer coefficients (α). All phase-field simulations were conducted using the COMSOL Multi-physics 5.5 platform. As depicted in Fig. 2f and h, there is minimal variation in the initial distribution of the current density on the substrate, regardless of the electrolyte used. Nevertheless, after cycling (Fig. 2g and i), the current density on the substrate of D-2NE is markedly lower and more uniform compared to BE. Additionally, the surface roughness of D-2NE exhibits relatively small changes (2.28 %) with a uniform morphology of K electrodeposition on the substrate. In contrast, the surface roughness dramatically increased to 18.11 % in BE during electrodeposition (Fig. S7). These results indicate that D-2NE effectively modulates the distribution of current density on the substrate, facilitating the uniform deposition of K-metal during repeated electrodeposition cycles. This uniform distribution of K-ions is attributed to the electrodeposition of spherical K that results in the even growth of the potassium layer on the substrate.

The practical operation of KMBs under fast-charging conditions (high current density) is a significant challenge. Therefore, under high current density, we further examined the effects of the $NaNO_3$ additive on the electrodeposition of K-metals through a combination study that included SEM, atomic force microscopy (AFM), and *operando*-Optical microscopy (*o*-OM) analyses. SEM with a focused ion beam (FIB) was used to assess the electrodeposited K-metal at both the top and cross-sectional views. K-metal was deposited onto the Cu substrate at a capacity loading of 4 mAh cm^{-2} and current density of 12 mA cm^{-2}. Compared to observations in BE (Fig. 3a-b), D-2NE (Fig. 3c-d) produced a dendrite-free and densely packed electrodeposited K-metal film (BE: 14.4 μm and D-2NE: 6.9 μm) that was composed of thick K-metal particles. These observed patterns were distinctly confirmed through 2D and 3D AFM topographic analyses (scan size: 5 μm $\times$ 5 μm) of the deposited K. The color changes (from red to blue) in the 2D mapping images (Fig. S8) demonstrate drastic differences in the surface roughness of the deposited K. The 3D topographic maps, including the height profile of electrodeposited K (Fig. 3e–g) exhibited tortuous dendrites (height profile variation of $>$ 0.6 μm) and uniform deposits of K-metal (height profile variation of $<$ 0.2 μm) for BE and D-2NE, respectively.

o-OM was further conducted to unravel the different electrodeposition mechanisms of K-metal between BE and D-2NE (Fig. 4). Over 5 min, *o*-OM monitored the K deposition process at a constant current of 12 mA cm^{-2} using customized K/K cells in real-time. Fig. 4 compares the snapshot images from recorded videos in electrolytes with and without $NaNO_3$ additive (Supporting video 1: BE and Supporting video 2: D-2NE). In the case of the BE, the formation of K dendrites began only after 1 min, with the dendrite growth rate increasing until a hard short-circuit occurred after 5 min (Fig. 4a). By contrast, no visible K dendrites were observed for the first 2 min in D-2NE. Although K dendrites were inevitably developed in D-2NE after 3 min due to the extremely high current density, the growth rate was significantly slower than that of BE. The impact of $NaNO_3$ on retarding the dendritic growth of K-metal was

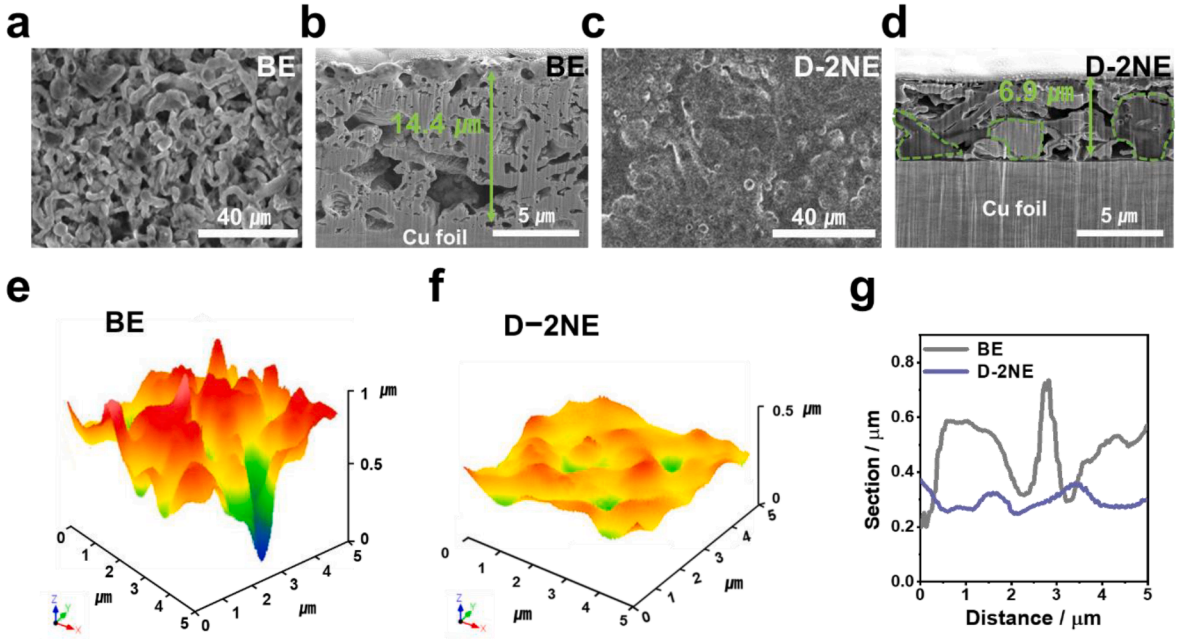

Fig. 3. (a and c) SEM and (b and d) FIB images of electrolytes at a current density of 12 mA cm^{-2} and capacity loading of 4 mAh cm^{-2}: (a and b) BE and (c and d) D-2NE. (e and f) 3D AFM topographic images (5 $\times$ 5 μm^2 scan size) and (g) height profiles of electrodeposited K on the Cu substrate at a current density of 12 mA cm^{-2} and capacity loading of 4 mAh cm^{-2} in (e) BE and (f) D-2NE.

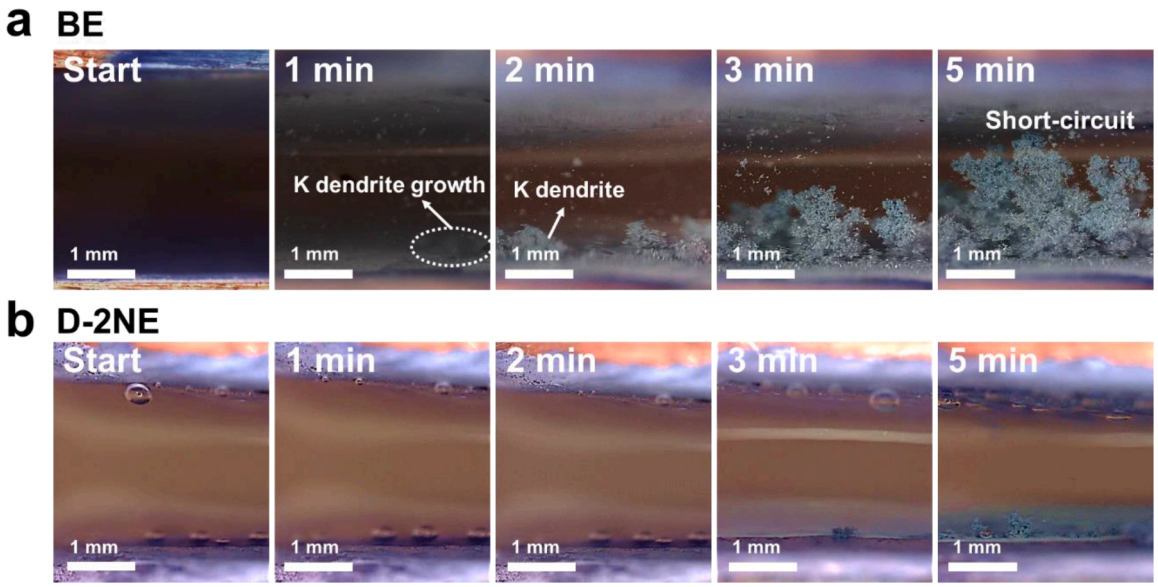

Fig. 4. Snapshots of *operando*-Optical microscopy analysis of the electrochemical deposition of K in (a) BE and (b) D-2NE.

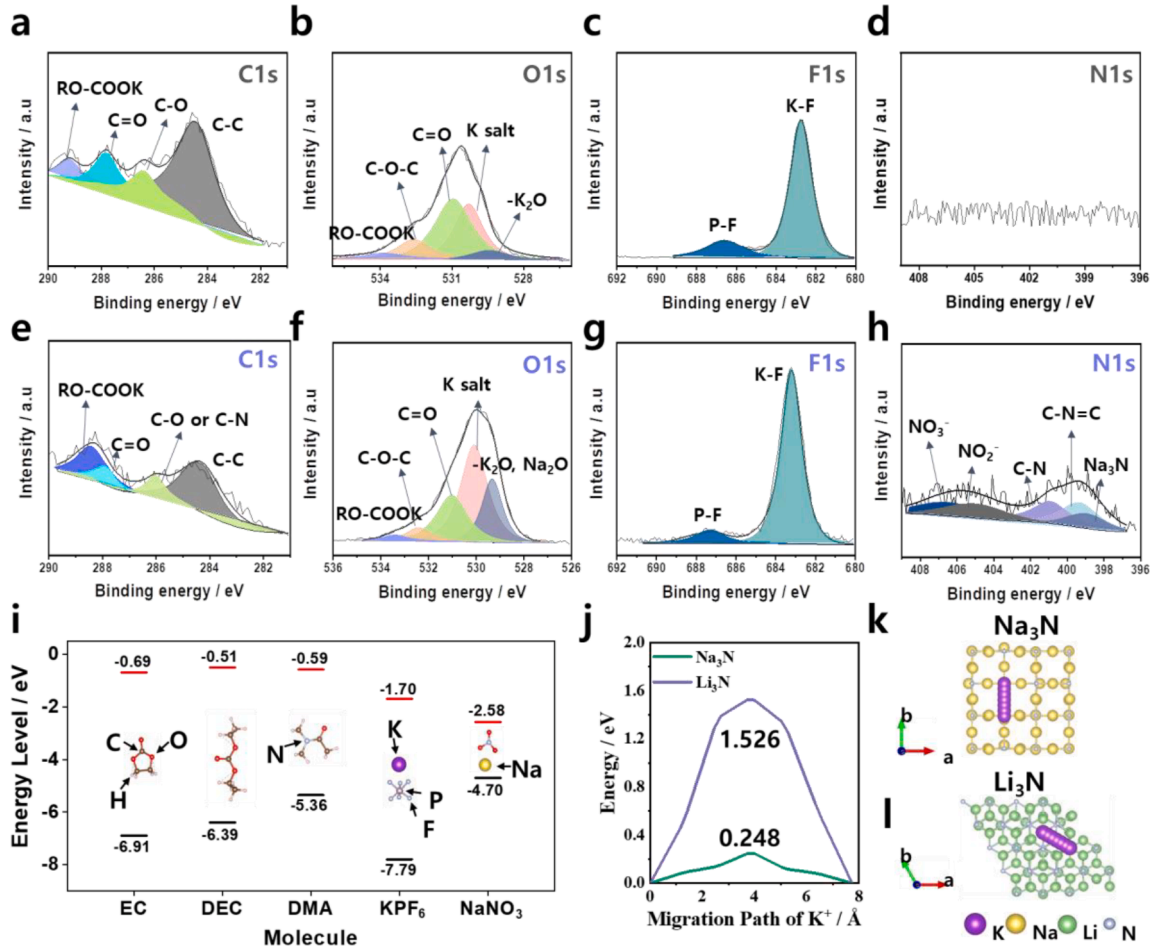

Fig. 5. Characterization of the chemical components of the SEI layer formed on the Cu foil in (a–d) BE and (e–h) D-2NE. XPS spectra of (a and e) C1s, (b and f) O1s, (c and g) F1s, and (d and h) N1s at a current density of 1 mA cm^{-2} and capacity loading of 1 mAh cm^{-2}. (i) HOMO–LUMO energy levels of the salt (KPF_6 and $NaNO_3$) and solvents (EC, DEC, and DMA). NEB energetic profiles for the migration pathways of K^+ are presented in (j). (j) describes minimum energy pathways (MEPs), and (k and l) illustrate the most probable K–ion migration paths for Na_3N and Li_3N, respectively.

additionally supported by *o*-OM data obtained using D-BE (Fig. S9, Supporting video 3: D-BE). The combined SEM, AFM, and *o*-OM analysis data provided solid evidence for the beneficial effects of the $NaNO_3$ additive in carbonate-based electrolytes to suppress the formation of K dendrite and its growth during plating reactions.

The distinct electrodeposit behaviors of K-metal between BE and D-2NE are attributed to the chemical properties of the SEI layer. Using X-ray photoelectron spectroscopy (XPS) analysis, we characterized the chemical composition of SEI layers retrieved from K/Cu cells with and without the using the $NaNO_3$ additive (Fig. 5). Understanding the highest occupied molecular orbital (HOMO) and lowest unoccupied molecular orbital (LUMO) energies of the salts and solvents is crucial for investigating the chemical components of the SEI layer, as the electrolyte solution inevitably decomposes at the metallic anode surface during the plating process. Density functional theory (DFT) calculations were conducted to determine the HOMO and LUMO energies of the salts (KPF_6 and $NaNO_3$) and solvents (EC, DEC, and DMA). Fig. 5i indicates that $NaNO_3$ possesses the lowest LUMO energy compared to that of other components in the electrolyte solution. This suggests that $NaNO_3$ is preferentially reduced on the surface of the K-metal anode during the D-2NE plating process, thus contributing to the formation of the inorganic components derived from NO_3^- in the SEI layer [55,23] (see the N 1s spectra in Fig. 5d and h). Notably, the formation of K_3N from the redox reaction of N^{3-} is inherently unstable [56]. Conversely, the formation energy of Na_3N is energetically stable (ΔH_f = -63.518 kJ/mol) via the spontaneous reaction of $3Na^+ + N^{3-} \rightarrow Na_3N$ [57]. Therefore, we reasonably believed that the N^{3-} species observed in N 1s spectra were more likely to be Na_3N rather than K_3N. Note that the peaks at 285.4 eV and 400.1 eV corresponding to C-N compound in the C 1s and N 1s spectra, respectively were attributed to the electrochemical reduction of DMA [58–61]. Additionally, nudged elastic band (NEB) calculations revealed that Na_3N (0.261 eV) can provide good K^+ diffusion channels in the crystal structure that contribute to the uniform electrodeposition of K-metal rather than to dendritic growth (Fig. 5j–l). F 1s spectra confirmed that D-2NE produced a relatively large fraction of K-F and P-F derivatives compared to those of BE, as the introduction of $NaNO_3$ triggers the facile reduction of PF_6^- by weakening the K^+-PF_6^- bonding in the electrolyte solution (Fig. 5c and g). Furthermore, noticeable differences in inorganic species such as K salt, K_2O, and Na_2O were observed between BE and D-2NE in the O 1s spectra, thus indicating that the addition of $NaNO_3$ additive triggers the formation of inorganic K_2O and/or Na_2O in the SEI layer [62]. The $NaNO_3$ additive preferentially decomposes over salts and solvents in the electrolyte solution during the plating process. This not only prevents the decomposition of extra solvent molecules but also leads to the formation of an inorganic-rich SEI layer [63,64]. This further verified by C 1s, O 1s, and F 1s XPS spectra with different etching time of 0s (outmost surface) and 60s (inner part) (Fig. S10). The outmost surface of SEI layer formed from BE and D-2NE electrolytes shows the marginal differences for the KF compound. However, when etching progresses into the inner part of SEI layer, D-2NE has the lower contents of organic species but higher KF content compared to BE (relative intensity in the SEI layer); this indicated that the addition of 0.02 M $NaNO_3$ additive reduce the decomposition of solvent molecules with forming the large fraction of inorganic F-rich compounds [58–61,65–68]. Overall, these features can enhance the mechanical integrity of the SEI layer and suppress the dissolution of organic species in the SEI layer by polar molecules in electrolyte solutions. The mechanical strength of the SEI layer was evaluated using AFM force-displacement (F/D) measurements (Fig. S11a and b) [69,70]. Both electrolytes exhibited typical F/D curves of the SEI layer; however, the SEI layer induced by D-2NE revealed a relatively higher Young's modulus (6.578 GPa) compared to that of BE (4.869 GPa). This implies that the introduction of $NaNO_3$ can effectively suppress volume changes during K plating/stripping and is resistant to dendrite growth [71]. The dissolution of the SEI layer in the electrolyte solution was experimentally quantified using K/Cu cells (Fig. S12). The cells were cycled in the voltage range of 0.005–2.0 V. The cells were paused at 2 V for different holding times (50, 30, 15, and 5 h) every five cycles to illustrate SEI dissolution, and they were then subjected to further cycling [72]. The capacity increment after each pause indicated the formation of a new SEI layer at the anode surface to compensate for the dissolution of the former SEI layer via reduction reactions in the electrolyte solution. Therefore, the difference in the capacity before and after each pause can be used to quantify the SEI dissolution in each electrolyte. Notably, the D-2NE always exhibited a lower degree of SEI dissolution compared to that of BE. This can be attributed to the dendrite-free electrodeposition of K-metal as well as the ability of inorganic-rich chemical compounds to suppress the breakdown of the SEI layer during repeated plating/stripping reactions.

The important functions of the $NaNO_3$ additive (D-2NE) in stabilizing the K-metal anode are illustrated in Fig. 6, compared to the function of BE based on comprehensive analysis. The positive effects of the $NaNO_3$ additive for enhancing the stability of K-metal anodes in carbonate electrolytes have been experimentally demonstrated in various electrochemical cells. Initially, the Coulombic efficiency (CE) of BE and D-2NE was evaluated in the K/Cu cells using the advanced method proposed by Zhang et al. [73]. The method is designed for obtaining reliable plating/stripping reactions of K-metal in K/Cu asymmetric cells by minimizing the influence of the Cu substrate in the first electrodeposition reaction. Voltage–time plots of the K/Cu cells are presented in Fig. S13. The CEs values were calculated after 30 cycles using the following equation:

$$CE_{avg} = \frac{nQ_C + Q_S}{nQ_C + Q_T} \quad (2)$$

where a charge capacity (Q_T) of 4 mAh cm^{-2} was used to deposit K onto the Cu substrate that served as a K reservoir. Subsequently, 0.4 mAh cm^{-2} of this charge capacity (Q_c) was used to cycle K between the working and counter electrodes for 30 cycles at a current density of 0.4 mA cm^{-2}. After 30 cycles, a final exhaustive stripping of electrodeposited K-metal was performed at a cut-off voltage of 1.0 V for 100 h, and the corresponding final stripping charge capacity (Q_S) was measured. D-2NE displayed an improved CE value of 90 % compared to that of BE (86.7 %). From the K/Cu cells, we obtained the Nyquist plots at the 30th cycle and calculated the diffusion coefficient using the following equation [74,75]:

$$D_{K+}(\text{diffusion coefficient}) = R^2T^2 / 2A^2n^4F^4C^2\partial^2 \quad (3)$$

where R is the ideal gas constant; T is the absolute temperature; A is the surface area of the electrode; n is the number of electrons transferred; F is Faraday's constant; C is the K-ion concentration; and ∂ is the Warburg constant. The D_{K+} values of BE and D-2NE are 1.5939×10^{-7} cm^2 S^{-1} and 3.01467×10^{-7} cm^2 S^{-1}, respectively. From the XPS data, it is believed that the improved D_{K+} of D-2NE can be attributed to the presence of ionically conductive Na_3N as well as a larger fraction of K_2O compounds in the SEI layer [63]. The cycling stability of K-metal anodes in BE and D-2NE were evaluated using symmetric K/K cells (with only one polymer separator) at a capacity loading of 4 mAh cm^{-2} and a current density of 12 mA cm^{-2}, and the resulting data were compared in Fig. 7a. Even under an extremely high current density, the K/K cell using D-2NE demonstrated a long lifespan of over 1000 h (1500 cycles). In contrast, the cell using BE exhibited very unstable signals in the time–voltage plot from the beginning of the cycle and eventually faced a hard short-circuit after only 200 cycles with large polarizations. Compared to BE, surprisingly, D-2NE also showed the outstanding rate performance up to 5 C rate (20 mA cm^{-2}) in the symmetric K/K cell with capacity loading of 4 mAh cm^{-2} (Fig. S14).

The important discovery of this study involves dissolving the $NaNO_3$ additive and thereby enhancing the K-metal stability in high-voltage carbonate-based electrolyte. Therefore, the effectiveness of $NaNO_3$ was further tested in full-cells using a Prussian blue-type $FeFe(CN)_6$

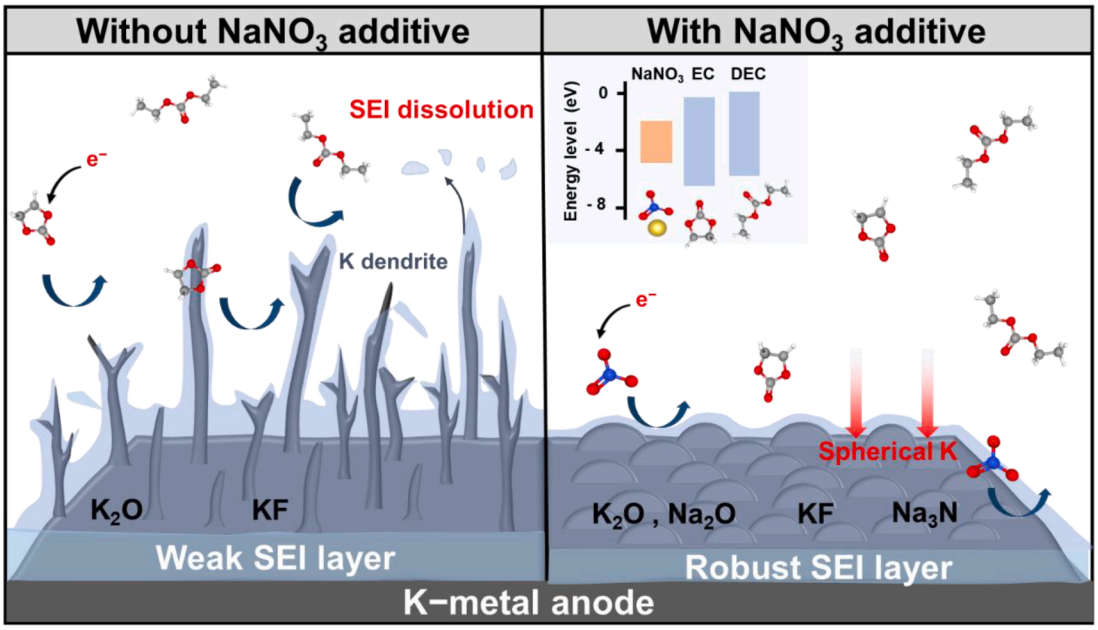

Fig. 6. Schematic of the $NaNO_3$ additive effect for the K-metal anode via an advanced SEI layer with higher mechanical and ionic conductivity.

cathode at high-voltage. $FeFe(CN)_6$ (FeHCF) was synthesized via a precipitation reaction [76]. X-ray diffraction patterns of FeHCF confirm that all diffraction peaks are indexed to cubic-phase PB analogs. The SEM images reveal the presence of nanoparticles possessing an average diameter of 20–40 nm. SEM and corresponding EDX mapping revealed uniform elemental distributions of Fe, N, and C in the nanoparticles (Fig. S15) [76,77]. Fig. 7b compares the electrochemical properties of FeHCF/K full-cells depending on the use of different electrolyte solutions in the voltage range of 1.5–4.0 V (vs. K/K^+) at a capacity loading of 1 mAh cm^{-2}. The full-cells delivered nearly identical 1st discharge capacities at 1 mA cm^{-2} in both electrolytes. The full-cell with D-2NE exhibited a high discharge capacity of 60 mAh g^{-1} and excellent cycle life over 600 cycles. In contrast, the full-cell with BE delivered low discharge capacity of 40 mAh g^{-1} and poor cycling stability with unstable CE after 200 cycles (Fig. 7c). To understand the primary reason for the drastic differences in cycling behaviors, full-cells with different electrolytes were cycled 200 times and disassembled after the end of discharge (K-stripped state). The *ex-situ* XRD patterns of the cycled cathode obtained from full-cells indicated no change in the original crystal structure in either electrolyte (Fig. 7d). Conversely, the cycled K-metal anode indicates that the poor cycling performance of the full-cell in BE can be attributed to the degradation of cycled K-metal. This hypothesis is supported by SEM analysis of the cycled K-metal and cycled separator (Fig. 7e). In the case of BE, many pores in the cycled separator are blocked due to the internal short-circuit caused by dendritic growth of K-metal (see the cycled K-metal) during cycling. In contrast, the K-metal surface and cycled separator for the full-cell with D-2NE possessed a smooth surface. These observations clearly demonstrate that D-2NE can effectively stabilize the K-metal anode in the full-cells by delaying the anode degradation, thereby yielding long-term cycling stability of KMBs.

3. Conclusion

In this study, we reported a significant discovery of dissolving $NaNO_3$ additives using DMA as a mediator solvent in a carbonate-based electrolyte (0.5 M KPF_6 in EC:DEC) for high performance KMBs. The reduction of $NaNO_3^-$ produced an ionically conductive SEI layer with the Na_3N compound and altered the morphology of electrodeposited K-metal from dendritic fibers to spherical particles. These unique features contribute to lowering the nucleation potential of K^+ and make K-metal highly resistant to dendrite formation, even at high current densities. By using $NaNO_3$ additive in a carbonate-based electrolyte, the K-metal anode survived long-term cycling in both the K/K symmetric cell and high-voltage full-cells using the FeHCF cathode under high capacity loading and high current density. We believe that the proposed modulation strategy of the carbonate-based electrolyte, facilitated by introducing the $NaNO_3$ additive with a solubility mediator and provides new insights for improving the energy density and lifetime of KMBs.

4. Experimental section

4.1. Electrolyte preparation

The KPF_6 and $NaNO_3$ salts were dried under a vacuum at 110 °C in a vacuum oven (Buchi). EC:DEC (volume ratio, 1:1; Dongwha Electrolyte Engineering) and DMA (Alfa Aesar) solvent were purified using vacuum–dried 4 Å molecular sieves over the course of 3 days. BE was prepared using 0.5 mol L^{-1} KPF_6 (TCI) dissolved in EC:DEC. The 0.02 M $NaNO_3$ was dissolved in D–BE composed of BE:DMA (weight ratio, 38.5:1).

4.2. Preparation of the cathode

FeHCF powder was synthesized using potassium hexacyanoferrate ($K_3Fe[CN]_6$, 99 %; Aldrich) and iron (III) chloride hexahydrate ($FeCl_3$, 99.9 %; Aldrich). A 50 mL volume of 0.1 mol L^{-1} $K_3Fe(CN)_6$ aqueous solution was added to 100 mL of 0.1 mol L^{-1} $FeCl_3$ aqueous solution with stirring and then maintained at 60 °C for 6 h. After natural cooling to room temperature, a green precipitate was obtained by centrifugation, and it was washed several times with deionized water and dried in an oven at 80 °C overnight. The electrode was prepared by casting the active material (60 wt. %), Super P (30 wt.%), and the mixture of 10 wt. % poly (vinylidene fluoride) (PVDF, average M_w of ~534,000 by GPC; Aldrich) in a 1-methyl-2-pyrrolidone (NMP, 99.5 %; Daejung Chemicals) binder slurry (10 wt.%) on carbon-coated Al foil. The cathode was vacuum-dried at 70 °C for 12 h.

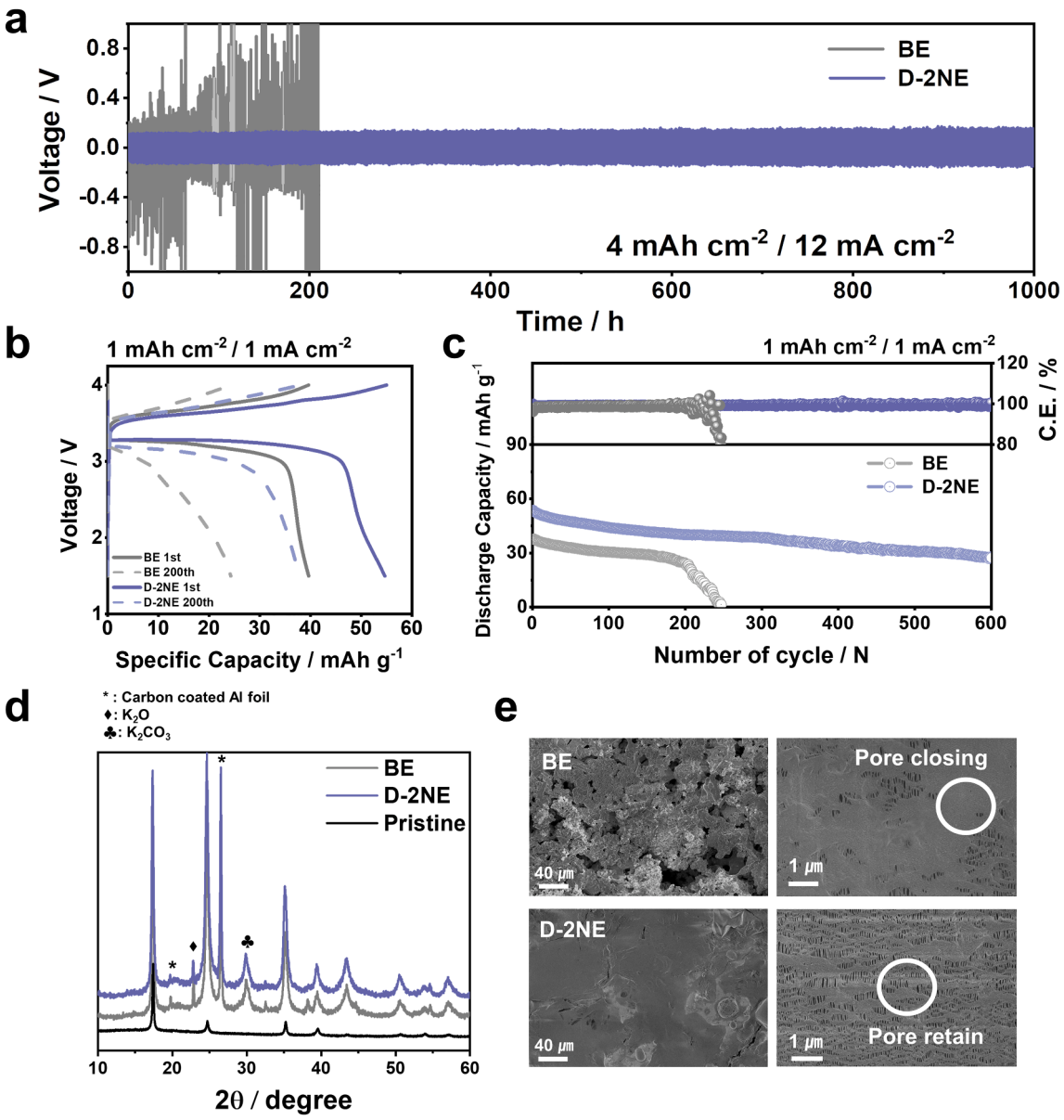

Fig. 7. (a) Galvanostatic cycling performances for K/K symmetric cells at a current density of 12 mA cm^{-2} and capacity loading of 4 mAh cm^{-2} in BE and D-2NE using a single separator. (b) Charge-discharge voltage profiles of K/FeHCF full-cells in the voltage range of 1.5–4.0 V at a current density of 1 mA cm^{-2} and capacity loading of 1 mAh cm^{-2} in BE and D-2NE. (c) Cycling performances of the full-cells in the electrolytes corresponding to (b). (d) *Ex–situ* XRD patterns of the cycled FeHCF cathode obtained from K/FeHCF full-cells in Fig. 7c. (e) SEM images corresponding to cycled K-metal anodes and separators (polymer membrane) obtained from K/FeHCF full-cells in Fig. 7c for the (a) BE and (b) D–2NE.

4.3. Electrochemical measurements

Electrochemical measurements were performed using 2032 coin cells assembled in an Ar-filled glove box (O_2, H_2O < 0.1 ppm). Symmetric cells were assembled with K-foil (15 mm diameter), polymer separator (Celgard 2400), and 100 μL of electrolyte. Each cell was measured under galvanostatic cycling conditions at a current density of 12 mA cm^{-2} and capacity loadings of 4 mAh cm^{-2} using VMP3 (Biologic). Electrochemical impedance spectra (EIS) were obtained on an asymmetric K/Cu cell in the frequency range of 1 MHz-1 mHz with a perturbation amplitude of 14.2 mV using VMP3 (Biologic). The full–cell of K-metal/FeHCF was conducted in the constant-current mode at a current density of 0.5 mA cm^{-2} and capacity loading of 0.5 mAh cm^{-2} using TOSCAT in the voltage range of 1.5–4.0 V (K/K^+). In addition to cycling performances, the rate performance was assessed at various current densities of 0.18, 0.54, 0.9, and 1 mA cm^{-2} and a capacity loading of 1 mAh cm^{-2}.

4.4. Characterization

The solvated structure of the electrolyte was confirmed by NMR spectrometry (600 MHz, Agilent DD2 NMR). Field-emission scanning electron microscopy (Helios NanoLab 600) with EDX mapping verified the morphologies and elemental distributions of the K-metal anode and FeHCF cathode were confirmed by. Along with the SEM analysis, FIB (Helios NanoLab 600) was employed for cross-section of the electrodeposited K on the Cu foil. *Operando*-Optical microscopy platform (VHX-7000) with customized cell using a Potentiostat (VMP3) captured dendritic growth of the K-metal anode. Compounds formed on the SEI layer were characterized via high-performance X-ray photoelectron spectroscopy (HP-XPS, K–LPHA+). AFM-based characterizations were performed using a high-resolution AFM (HR–AFM) scanning probe

microscope (Probes) in an Ar–gas–filled glovebox unless otherwise specified. Non-contact mode images of the surface morphology were obtained using silicon AFM tip–coated Al (PR-T190, Probes) at a typical scan rate of 0.5 Hz. The force curves of the samples were obtained in contact mode using a silicon probe–coated diamond (CDT-NCLR) with a spring constant of 7.2 N. Equation for calculating Young's modulus was derived using the Hertz model from the references of Derjaguin et al. and Barthel et al.[69,70], as follow:

$$F = \frac{4}{3}\frac{E}{\left(1-\theta^2\right)}\sqrt{R}(d_{max}-d)^{\frac{3}{2}} - F_{max} \quad (4)$$

where E, θ, d, F and R are respectively the Young's modulus of the surface, the Poisson's factor of the surface (0.5), adhesion distance, adhesion force and the curvature radius of the probe (ca. 10 nm), respectively, and the $d_{max}$and $F_{max}$are point of maximal adhesion distance and adhesion force for retract curve. For the SEI dissolution test, Cu (19 mm diameter), K (15 mm diameter), PP separators (19 mm diameter, Celgard 2400), and 100 μL of electrolyte were cycled in the voltage range of 0.005–2.0 V at a constant current of 3 μA cm^{-2}. The K/FeHCF full–cells were tested in the voltage range of 1.5–4.0 V at 1C (1 C = 120 mAh g^{-1}) using a battery tester (TOSCAT). The morphologies of the cycled K, polymer separator, and structures of the cathode materials obtained from the cycled cells were observed by FE-SEM (Helios) and X–ray diffraction (XRD, Bruker).

4.5. Multi-physics simulation

The distribution of the current densities and concentration fields on the surface of the K electrode during the electrodeposition process was simulated using the finite element method in COMSOL Multi-physics. The local current density on the K electrode was determined using the Butler–Volmer equation, and it was influenced by the local concentration distribution, temperature, and electrochemical reaction rate. The concentration field of K-ion on the electrode surface, as determined by Fick's second law in three dimensions, is given as:

$$\frac{\partial c_{k^+}}{\partial \Gamma} = D\nabla^2 c_{k^+} \quad (5)$$

where D is the diffusion coefficient of K-ion in liquid electrolyte. The flux of K-ion in electrolyte is determined by the Nernst–Planck equation:

$$N = -D\nabla c_{k^+} - q_{k^+}u_{k^+}Fc_{k^+}\nabla\varphi \quad (6)$$

where N is the transfer vector of species, u_i is the ionic mobility, and φ is the electrolyte potential. During the electrodeposition process of K, the K-ions are reduced to K atoms, and this conversion process is described as:

$$\frac{\partial c_{k^+}}{\partial t} + \nabla\cdot\vec{N} = 0 \quad (7)$$

The finite element simulation is conducted on a bulk K-metal model with an area of 50 μm × 50 μm and a thickness of 20 μm as presented in Fig. S5. A random roughness was built on the K electrode surface to simulate the initial morphology. Ultra-fine grid division with a grid size of 0.015 μm were applied to the model to obtain high-precision results.

4.6. Computational methods

Theoretical calculations of the HOMO–LUMO energy levels were performed using the Gaussian 09 package. Geometry optimization of the molecules was conducted using the closed-shell Perdew–Burke–Ernzerhof (PBE) generalized gradient approximation (GGA) method with the M06-2x/6-311+G(d,p) basis set [78]. To compute the minimum energy pathways (MEPs) using the nudged elastic band (NEB) method [79], we utilized the Vienna ab initio simulation package (VASP) [80–82] within the generalized gradient approximation (GGA) framework with the PBE function [83]. To enhance precision, the projection–augmented wave method (PAW) was employed to model the interactions between ions and electrons [84]. In this context, we considered 10^{-6} eV and 0.02 eV/Å as convergence criteria for energy and force, respectively. For the calculations, a 400-eV energy cut off and an 8 × 8 × 1 k-point mesh with a 0.05 eV Gaussian convolution were employed. The selected structures (Na_3N and Li_3N) adhered to Pm-3m and P6/m mm space-group symmetries, respectively [85].

CRediT authorship contribution statement

Jimin Park: Writing – original draft, Visualization, Data curation, Conceptualization. **Hyokyeong Kang:** Writing – original draft, Resources, Investigation, Formal analysis. **Marco Agostini:** Writing – review & editing, Validation. **Shizhao Xiong:** Software, Data curation. **Shivam Kansara:** Validation, Software. **Xieyu Xu:** Software, Investigation. **Yangyang Liu:** Software, Data curation. **Jang–Yeon Hwang:** Writing – review & editing, Supervision, Conceptualization.

Declaration of competing interest

The authors declare that they have no known competing financial interests or personal relationships that could have appeared to influence the work reported in this paper.

Supplementary materials

Supplementary material associated with this article can be found, in the online version, at doi:10.1016/j.ensm.2024.103443.

References

[1] C. Liu, S. Luo, H. Huang, Z. Wang, A. Hao, Y. Zhai, Z. Wang, $K_{0.67}Ni_{0.17}Co_{0.17}Mn_{0.66}O_2$: A cathode material for potassium-ion battery, Electrochem. Commun 82 (2017) 150, https://doi.org/10.1016/j.elecom.2017.08.008.
[2] C. Wei, Y. Tao, H. Fei, Y. An, Y. Tian, J. Feng, Y. Qian, Recent advances and perspectives in stable and dendrite-free potassium metal anodes, Energy Storage Mater. 30 (2020) 206–227, https://doi.org/10.1016/j.ensm.2020.05.018.
[3] H. Wang, J. Dong, Q. Guo, W. Xu, H. Zhang, K.C. Lau, Y. Wei, J. Hu, D. Zhai, F. Kang, Highly stable potassium metal batteries enabled by regulating surface chemistry in ether electrolyte, Energy Storage Mater. 43 (2021) 526–532, https://doi.org/10.1016/j.ensm.2021.08.013.
[4] M. Wang, H. Zhang, J. Cui, S. Yao, X. Shen, T.J. Park, J.K. Kim, Recent advances in emerging nonaqueous K-ion batteries: from mechanistic insights to practical applications, Energy Storage Mater. 39 (2021) 305–346, https://doi.org/10.1016/j.ensm.2021.04.034.
[5] J. Asenbauer, T. Eisenmann, M. Kuenzel, A. Kazzazi, Z. Chen, D. Bresser, The success story of graphite as a lithium-ion anode material – fundamentals, remaining challenges, and recent developments including silicon (oxide) composites, Sustain. Energy Fuels 4 (2020) 5387–5416, https://doi.org/10.1039/d0se00175a.
[6] J. Park, Y. Jeong, H. Kang, T.Y. Yu, X. Xu, Y. Liu, S. Xiong, S. Lee, Y.K. Sun, J. Y. Hwang, A dual-functional electrolyte additive for high-performance potassium metal batteries, Adv. Funct. Mater. 33 (2023) 2304069, https://doi.org/10.1002/adfm.202304069.
[7] N. Xiao, G. Gourdin, Y. Wu, Simultaneous stabilization of potassium metal and superoxide in K–O_2 batteries on the basis of electrolyte reactivity, Angew. Chem. Int. Ed. 57 (2018) 10864–10867, https://doi.org/10.1002/anie.201804115.
[8] G. Zeng, S. Xiong, Y. Qian, L. Ci, J. Feng, Non-flammable phosphate electrolyte with high salt-to-solvent ratios for safe potassium-ion battery, J. Electrochem. Soc. 166 (2019) A1217–A1222, https://doi.org/10.1149/2.1171906jes.
[9] J. Park, G. Oh, U.H. Kim, M.H. Alfaruqi, X. Xu, Y. Liu, S. Xiong, A.T. Zikri, Y.K. Sun, J.Y. Hwang, Regulating the solvation structure of electrolyte via dual–salt combination for stable potassium metal batteries, Adv. Sci. 10 (2023) 2301201, https://doi.org/10.1002/advs.202301201.
[10] P. Liu, D. Mitlin, Emerging potassium metal anodes: perspectives on control of the electrochemical interfaces, Acc. Chem. Res. 53 (2020) 1161–1175, https://doi.org/10.1021/acs.accounts.0c00099.
[11] Y. Gao, Z. Hou, R. Zhou, D. Wang, X. Guo, Y. Zhu, B. Zhang, Critical roles of mechanical properties of solid electrolyte interphase for potassium metal anodes, Adv. Funct. Mater. 32 (2022) 2112399, https://doi.org/10.1002/adfm.202112399.
[12] Q. Zhang, B. Han, Y. Zou, S. Shen, M. Li, X. Lu, M. Wang, Z. Guo, J. Yao, Z. Chang, M. Gu, Enabling atomic-scale imaging of sensitive potassium metal and related

solid electrolyte interphases using ultralow-dose cryo-TEM, Adv. Mater. 33 (2021) 2102666, https://doi.org/10.1002/adma.202102666.
[13] S. Liu, J. Mao, Q. Zhang, Z. Wang, W.K. Pang, L. Zhang, A. Du, V. Sencadas, W. Zhang, Z. Guo, An intrinsically non-flammable electrolyte for high-performance potassium batteries, Angew. Chem. Int. Ed. 59 (2020) 3638–3644, https://doi.org/10.1002/anie.201913174.
[14] W. Liu, P. Liu, D. Mitlin, Review of emerging concepts in SEI analysis and artificial SEI membranes for lithium, sodium, and potassium metal battery anodes, Adv. Energy Mater. 10 (2020) 2002297, https://doi.org/10.1002/aenm.202002297.
[15] Y. Hu, L. Fan, A.M. Rao, W. Yu, C. Zhuoma, Y. Feng, Z. Qin, J. Zhou, B. Lu, Cyclic-anion salt for high-voltage stable potassium-metal batteries, Natl. Sci. Rev. 9 (2022) nwac134, https://doi.org/10.1093/nsr/nwac134.
[16] H. Sun, J. Zhu, D. Baumann, L. Peng, Y. Xu, I. Shakir, Y. Huang, X. Duan, Hierarchical 3D electrodes for electrochemical energy storage, Nat. Rev. Mater. 4 (2019) 45–60, https://doi.org/10.1038/s41578-018-0069-9.
[17] X. Tang, D. Zhou, P. Li, X. Guo, B. Sun, H. Liu, K. Yan, Y. Gogotsi, G. Wang, MXene-based dendrite-free potassium metal batteries, Adv. Mater. 32 (2020) 1906739, https://doi.org/10.1002/adma.201906739.
[18] M. Ye, J.Y. Hwang, Y.K. Sun, A 4 V class potassium metal battery with extremely low overpotential, ACS Nano 13 (2019) 9306–9314, https://doi.org/10.1021/acsnano.9b03915.
[19] Q. Liu, A.M. Rao, X. Han, B. Lu, Artificial SEI for superhigh-performance K-graphite anode, Adv. Sci. 8 (2021) 2003639, https://doi.org/10.1002/advs.202003639.
[20] Y. Liu, D. Lin, Y. Li, G. Chen, A. Pei, O. Nix, Y. Li, Y. Cui, Solubility-mediated sustained release enabling nitrate additive in carbonate electrolytes for stable lithium metal anode, Nat. Commun. 9 (2018) 365, https://doi.org/10.1038/s41467-018-06077-5.
[21] W. Li, H. Yao, K. Yan, G. Zheng, Z. Liang, Y.M. Chiang, Y. Cui, The synergetic effect of lithium polysulfide and lithium nitrate to prevent lithium dendrite growth, Nat. Commun. 6 (2015) 7436, https://doi.org/10.1038/ncomms8436.
[22] Z. Wang, Y. Wang, C. Wu, W.K. Pang, J. Mao, Z. Guo, Constructing nitrided interfaces for stabilizing Li metal electrodes in liquid electrolytes, Chem. Sci. 12 (2021) 8945, https://doi.org/10.1039/d1sc01806j.
[23] Z.L. Brown, S. Heiskanen, B.L. Lucht, Using triethyl phosphate to increase the solubility of $LiNO_3$ in carbonate electrolytes for improving the performance of the lithium metal anode, J. Electrochem. Soc. 166 (2019) A2523–A2527, https://doi.org/10.1149/2.0991912jes.
[24] X.Q. Zhang, T. Li, B.Q. Li, R. Zhang, P. Shi, C. Yan, J.Q. Huang, Q. Zhang, A sustainable solid electrolyte interphase for high-energy-density lithium metal batteries under practical conditions, Angew. Chem. Int. Ed. 59 (2020) 3252–3257, https://doi.org/10.1002/ange.201911724.
[25] C. Yan, Y.X. Yao, X. Chen, X.B. Cheng, X.Q. Zhang, J.Q. Huang, Q. Zhang, Lithium nitrate solvation chemistry in carbonate electrolyte sustains high-voltage lithium metal batteries, Angew. Chem. Int. Ed. 57 (2018) 14055–14059, https://doi.org/10.1002/anie.201807034.
[26] J. Fu, X. Ji, J. Chen, L. Chen, X. Fan, D. Mu, C. Wang, Lithium nitrate regulated sulfone electrolytes for lithium metal batteries, Angew. Chem. Int. Ed. 59 (2020) 22378–22385, https://doi.org/10.1002/anie.202009575.
[27] S-H. Wu, A. Huang, Effects of tris(Pentafluorophenyl) borane (TPFPB) as an electrolyte additive on the cycling performance of $LiFePO_4$ batteries, J. Electrochem. Soc. 160 (2013) A684–A689, https://doi.org/10.1149/2.074304jes.
[28] S. Liu, X. Ji, N. Piao, J. Chen, N. Eidson, J. Xu, P. Wang, L. Chen, J. Zhang, T. Deng, S. Hou, T. Jin, H. Wan, J. Li, J. Tu, C. Wang, An inorganic-rich solid electrolyte interphase for advanced lithium-metal batteries in carbonate electrolytes, Angew. Chem. Int. Ed. 60 (2021) 3661–3671, https://doi.org/10.1002/anie.202012005.
[29] D. Liu, X. Xiong, Q. Liang, X. Wu, H. Fu, An inorganic-rich SEI induced by $LiNO_3$ additive for a stable lithium metal anode in carbonate electrolyte, Chem. Commun. 57 (2021) 9232–9235, https://doi.org/10.1039/d1cc03676a.
[30] L. Suo, W. Xue, M. Gobet, S.G. Greenbaum, C. Wang, Y. Chen, W. Yang, Y. Li, J. Li, Fluorine-donating electrolytes enable highly reversible 5-V-class Li metal batteries, PNAS 115 (2018) 1156–1161, https://doi.org/10.1073/pnas.1712895115.
[31] C. Yan, H.R. Li, X. Chen, X.Q. Zhang, X.B. Cheng, R. Xu, J.Q. Huang, Q. Zhang, Regulating the inner Helmholtz plane for stable solid electrolyte interphase on lithium metal anodes, J. Am. Chem. Soc. 141 (2019) 9422–9429, https://doi.org/10.1021/jacs.9b05029.
[32] R.A. Miranda-Quintana, J. Smiatek, Calculation of donor numbers: computational estimates for the Lewis basicity of solvents, J. Mol. Liq. 322 (2021) 114506, https://doi.org/10.1016/j.molliq.2020.114506.
[33] S. Sekhon, Effect of donor number of solvent on the conductivity behaviour of nonaqueous proton-conducting polymer gel electrolytes, Solid State Ion. 160 (2003) 301–307, https://doi.org/10.1016/S0167-2738(03)00167-X.
[34] A.A. Petrov, A.A. Ordinartsev, S.A. Fateev, E.A. Goodilin, A.B. Tarasov, Solubility of Hybrid Halide Perovskites in DMF and DMSO, Molecules 26 (2021) 7541, https://doi.org/10.3390/molecules26247541.
[35] N. Nambu, R. Takahashi, M. Takehara, M. Ue, Y. Sasaki, Electrolytic characteristics of fluoroethylene carbonate for electric double-layer capacitors at high concentrations of electrolyte, Electrochemistry 81 (2013) 817, https://doi.org/10.5796/electrochemistry.81.817.
[36] H. Chu, H. Noh, Y.J. Kim, S. Yuk, J.H. Lee, J. Lee, H. Kwack, Y. Kim, D.K. Yang, H. T. Kim, Achieving three-dimensional lithium sulfide growth in lithium-sulfur batteries using high-donor-number anions, Nat. Commun. 10 (2019) 188, https://doi.org/10.1038/s41467-018-07975-4.
[37] Q. Sun, Z. Cao, Z. Ma, J. Zhang, W. Wahyudi, G. Liu, H. Cheng, T. Cai, E. Xie, L. Cavallo, Q. Li, J. Ming, Interfacial and interphasial chemistry of electrolyte, components to invoke high-performance antimony, anodes and non-flammable lithium-ion batteries, Adv. Funct. Mater. 33 (2023) 2210292, https://doi.org/10.1002/adfm.202210292.
[38] C.C. Su, M. He, C. Peebles, L. Zeng, A. Tornheim, C. Liao, L. Zhang, J. Wang, Y. Wang, Z. Zhang, Functionality selection principle for high voltage lithium-ion battery electrolyte additives, ACS Appl. Mater. Interfaces 9 (2017) 30686–30695, https://doi.org/10.1021/acsami.7b08953.
[39] C. Xu, G. Hernandez, S. Abbrent, L. Kobera, R. Konefal, J. Brus, K. Edstrom, D. Brandell, J. Mindemark, Unraveling and mitigating the storage instability of fluoroethylene carbonate-containing $LiPF_6$ electrolytes to stabilize lithium metal anodes for high-temperature rechargeable batteries, ACS Appl. Energy Mater. 2 (2019) 4925–4935, https://doi.org/10.1021/acsaem.9b00607.
[40] P. Biswas, P. Ghildiyal, H. Kwon, H. Wang, Z. Alibay, F. Xu, Y. Wang, B.M. Wong, M.R. Zachariah, Rerouting pathways of solid-state ammonia borane energy release, J. Phys. Chem. C 126 (2022) 48–57, https://doi.org/10.1021/acs.jpcc.1c08985.
[41] H. Cheng, Q. Sun, L. Li, Y. Zou, Y. Wang, T. Cai, F. Zhao, G. Liu, Z. Ma, W. Wahyudi, Q. Li, J. Ming, Emerging era of electrolyte solvation structure and interfacial model in batteries, ACS Energy Lett. 7 (2022) 490–513, https://doi.org/10.1021/acsenergylett.1c02425.
[42] W. Wahyudi, V. Ladelta, L. Tsetseris, M.M. Alsabban, X. Guo, E. Yengel, H. Faber, B. Adilbekova, A. Seitkhan, A.H. Emwas, M.N. Hedhili, L.J. Li, V. Tung, N. Hadjichristidis, T.D. Anthopoulos, J. Ming, Lithium-ion desolvation induced by nitrate additives reveals new insights into high performance lithium Batteries, Adv. Funct. Mater. 31 (2021) 2101593, https://doi.org/10.1002/adfm.202101593.
[43] G. Liu, Z. Cao, L. Zhou, J. Zhang, Q. Sun, J.Y. Hwang, L. Cavallo, L. Wang, Y.K. Sun, J. Ming, Additives engineered nonflammable electrolyte for safer potassium ion batteries, Adv. Funct. Mater. 30 (2020) 2001934, https://doi.org/10.1002/adfm.202001934.
[44] Y. Han, A.P.V. Vijaya Kumar Saroja, H.R. Tinker, Y. Xu, Interphases in the electrodes of potassium ion batteries, J. Phys. Mater. 5 (2022) 022001, https://doi.org/10.1088/2515-7639/ac5dce.
[45] R. Zhao, X. Li, Y. Si, W. Guo, Y. Fu, Tuning solvation behavior of ester-based electrolytes toward highly stable lithium-metal batteries, ACS Appl. Mater. Interfaces 13 (2021) 40582–40589, https://doi.org/10.1021/acsami.1c10279.
[46] J. Wu, Z. Gao, Y. Tian, Y. Zhao, Y. Lin, K. Wang, H. Guo, Y. Pan, X. Wang, F. Kang, N. Tavajohi, X. Fan, B. Li, Unique tridentate coordination tailored solvation sheath toward highly stable lithium metal batteries, Adv. Mater. 35 (2023) 2303347, https://doi.org/10.1002/adma.202303347.
[47] X. Ma, J. Yu, X. Zou, Y. Hu, M. Yang, F. Zhang, F. Yan, Single additive to regulate lithium-ion solvation structure in carbonate electrolytes for high-performance lithium-metal batteries, Cell Rep. Phys. Sci. 4 (2023) 101379.
[48] S.H. Lee, J.J.Y. Hwang, J. Ming, Z. Cao, H.A. Nguyen, H.G. Jung, J. Kim, Y.K. Sun, Toward the sustainable lithium metal batteries with a new electrolyte solvation chemistry, Adv. Energy Mater. 10 (2020) 2000567, https://doi.org/10.1002/aenm.202000567.
[49] X.W. Sun, X.Y. Zhang, Q.T. Ma, X.Z. Guan, W. Wang, J.Y. Luo, Revisiting the electroplating process for lithium-metal anodes for lithium-metal batteries, Angew. Chem. Int. Ed. 59 (2020) 6665–6674, https://doi.org/10.1002/anie.201912217.
[50] R. Zhao, X. Li, Y. Si, S. Tang, W. Guo, Y. Fu, $Cu(NO_3)_2$ as efficient electrolyte additive for 4 V class Li metal batteries with ultrahigh stability, Energy Storage Mater. 37 (2021) 1–7, https://doi.org/10.1016/j.ensm.2021.01.030.
[51] H. Wang, E. Matios, J. Luo, W. Li, Combining theories and experiments to understand the sodium nucleation behavior towards safe sodium metal batteries, Chem. Soc. Rev. 49 (2020) 3783, https://doi.org/10.1039/d0cs00033g.
[52] P. Biswal, S. Stalin, A. Kludze, S. Choudhury, L.A. Archer, Nucleation and early stage growth of Li electrodeposits, Nano Lett. 19 (2019) 8191–8200, https://doi.org/10.1021/acs.nanolett.9b03548.
[53] Y. Liu, X. Xu, M. Sadd, O.O. Kapitanova, V.A. Krivchenko, J. Ban, J. Wang, X. Jiao, Z. Song, J. Song, S. Xiong, A. Matic, Insight into the critical role of exchange current density on electrodeposition behavior of lithium metal, Adv. Sci. 8 (2021) 2003301, https://doi.org/10.1002/advs.202003301.
[54] Y. Liu, X. Xu, O.O. Kapitanova, P.V. Evdokimov, Z. Song, A. Matic, S. Xiong, Electro-chemo-mechanical modeling of artificial solid electrolyte interphase to enable uniform electrodeposition of lithium metal anodes, Adv. Energy Mater. 12 (2022) 2103589, https://doi.org/10.1002/aenm.202103589.
[55] H. Shin, M. Baek, A. Gupta, K. Char, A. Manthiram, J.W. Choi, Recent progress in high donor electrolytes for lithium–sulfur batteries, Adv. Energy Mater. 10 (2020) 2001456, https://doi.org/10.1002/aenm.202001456.
[56] T. Weller, R. Lochmann, W. Meiler, H.J. Koehler, Theoretical investigations of the interaction of isobutene with sodium ions, J. Phys. Chem. 86 (1982) 3269–3271, https://doi.org/10.1021/j100213a039.
[57] J. Park, Y. Jeong, M.H. Alfaruqi, Y. Liu, X. Xu, S. Xiong, M.G. Jung, H.G. Jung, J. Kim, J.Y. Hwang, Y.K. Sun, Stable solid electrolyte interphase for long-life potassium metal batteries, ACS Energy Lett. 7 (2021) 401–409, https://doi.org/10.1021/acsenergylett.1c02354.
[58] Z. Zhu, Z. Liu, R. Zhao, X. Qi, J. Ji, F. Yang, L. Qie, Y. Huang, Heterogeneous nitride interface enabled by stepwise-reduction electrolyte design for dense Li deposition in carbonate electrolytes, Adv. Funct. Mater. 32 (2022) 2209384, https://doi.org/10.1002/adfm.202209384.
[59] J. Lee, J. Heo, B. Lee, H. Cho, T. Kim, J. Lee, Enhancement in the adhesion properties of polycarbonate surfaces through chemical functionalization with organosilicon coupling agents, J. Mater. Sci. Mater. Electron. 30 (2019) 17773–17779, https://doi.org/10.1007/s10854-019-02128-9.
[60] N. Chen, Y. Zhou, S. Cao, R. Wang, W. Jiao, A novel strategy for loading metal cocatalysts onto hollow nano-TiO_2 inner surface with highly enhanced H_2 production activity, Green Energy Environ. 8 (2021) 509–518, https://doi.org/10.1016/j.gee.2021.07.002.

[61] C. Xie, S. Yang, X. Xu, J.W. Shi, C. Niu, Core-shell structured carbon nanotubes/N-doped carbon layer nanocomposites for supercapacitor electrodes, J. Nanopart. Res. 22 (2020) 1–7, https://doi.org/10.1007/s11051-019-4734-8.
[62] P. Shi, X. Wang, X. Cheng, Y. Jiang, Progress on designing artificial solid electrolyte interphases for dendrite-free sodium metal anodes, Batteries 9 (2023) 345, https://doi.org/10.3390/batteries9070345.
[63] W. Li, G.C.M. Araújo, R.H. Scheicher, A. Blomqvist, R. Ahuja, Z. Xiong, Y. Feng, P. Chen, Li^+ ion conductivity and diffusion mechanism in α-Li_3N and β-Li_3N, Energy Environ. Sci. 3 (2010) 1524–1530, https://doi.org/10.1039/C0EE00052C.
[64] X. Ji, S. Hou, P. Wang, X. He, N. Piao, J. Chen, X. Fan, C. Wang, Solid-state electrolyte design for lithium dendrite suppression, Adv. Mater. 32 (2020) 2002741, https://doi.org/10.1002/adma.202002741.
[65] D. Briggs, G. Beamson, Primary and secondary oxygen-induced C1s binding energy shifts in X-ray photoelectron spectroscopy of polymers, Anal. Chem. 64 (1992) 1729–1736, https://doi.org/10.1021/ac00039a018.
[66] H. Wang, D. Yu, X. Wang, Z. Niu, M. Chen, L. Cheng, W. Zhou, L. Guo, Electrolyte chemistry enables simultaneous stabilization of potassium metal and alloying anode for potassium-ion batteries, Angew. Chem. Int. Ed. 131 (2019) 16603–16607, https://doi.org/10.1002/anie.201908607.
[67] X. Wang, S. Li, W. Zhang, D. Wang, Z. Shen, J. Zheng, H.L. Zhuang, Y. He, Y. Lu, Dual-salt-additive electrolyte enables high-voltage lithium metal full batteries capable of fast-charging ability, Nano Energy 89 (2021) 106353, https://doi.org/10.1016/j.nanoen.2021.106353.
[68] B. Qin, A. Schiele, Z. Jusys, A. Mariani, T. Diemant, X. Liu, T. Brezesinski, R. J. Behm, A. Varzi, S. Passerini, Highly reversible sodiation of tin in glyme electrolytes: the critical role of the solid electrolyte interphase and its formation mechanism, ACS Appl. Mater. Interfaces 12 (2020) 3697–3708, https://doi.org/10.1021/acsami.9b20616.
[69] B.V. Derjaguin, V.M. Muller, Y.P. Toporov, Effect of contact deformations on the adhesion of particles, J. Colloid Interface Sci. 53 (1975) 314–326, https://doi.org/10.1016/0021-9797(75)90018-1.
[70] E. Barthel, Adhesive elastic contacts: JKR and more, J. Phys. D 41 (2008) 163001, https://doi.org/10.1088/0022-3727/41/16/163001.
[71] R. Pathak, K. Chen, A. Gurung, K.M. Reza, B. Bahrami, F. Wu, A. Chaudhary, N. Ghimire, B. Zhou, W.H. Zhang, Y. Zhou, Q. Qiao, Ultrathin bilayer of graphite/SiO_2 as solid interface for reviving Li metal anode, Adv. Energy Mater. 9 (2019) 1901486, https://doi.org/10.1002/aenm.201901486.
[72] Y. Jin, P.M.L. Le, P. Gao, Y. Xu, B. Xiao, M.H. Engelhard, X. Cao, T.D. Vo, J. Hu, L. Zhong, B.E. Matthews, R. Yi, C. Wang, X. Li, J. Liu, J.G. Zhang, Low-solvation electrolytes for high-voltage sodium-ion batteries, Nat. Energy 7 (2022) 718–725, https://doi.org/10.1038/s41560-022-01055-0.
[73] B.D. Adams, J. Zheng, X. Ren, W. Xu, J.G. Zhang, Accurate determination of coulombic efficiency for lithium metal anodes and lithium metal batteries, Adv. Energy Mater. 8 (2018) 1702097, https://doi.org/10.1002/aenm.201702097.
[74] Y. Sun, J. Tang, K. Zhang, X. Yu, J. Yuan, D.M. Zhu, K. Ozawa, L.C. Qin, Effect of porous structural properties on lithium-ion and sodium-ion storage: illustrated by the example of a micro-mesoporous graphene $_{1-x}(MoS_2)_x$ anode, RSC Adv. 11 (2021) 34152, https://doi.org/10.1039/d1ra05179b.
[75] Y. Sun, C. Xu, B. Li, J. Xu, Y. He, H. Du, F. Kang, Synthesis of single-crystalline $LiMn_2O_4$ with different dimensional nanostructures for Li-ion batteries, Int. J. Electrochem. Sci. 9 (2014) 6387–6401, https://doi.org/10.1016/S1452-3981(23)10896-0.
[76] Z. Shadike, D.R. Shi, T. Tian-Wang, M.H. Cao, S.F. Yang, J. Chen, Z.W. Fu, Long life and high-rate Berlin green FeFe(CN)6 cathode material for a non-aqueous potassium-ion battery, J. Mater. Chem. A 5 (2017) 6393, https://doi.org/10.1039/c7ta00484b.
[77] X. Wu, W. Deng, J. Qian, Y. Cao, X. Ai, H. Yang, Single-crystal $FeFe(CN)_6$ nanoparticles: a high capacity and high rate cathode for Na-ion batteries, J. Mater. Chem. A 1 (2013) 10130, https://doi.org/10.1039/c3ta12036h.
[78] D.E. Woon, T.H. Dunning Jr, Gaussian basis sets for use in correlated molecular calculations.V. Core-valence basis sets for boron through neon, J. Chem. Phys. 103 (1995) 4572–4585, https://doi.org/10.1063/1.470645.
[79] B. Zhu, D.O. Scanlon, Predicting lithium iron oxysulfides for battery cathodes, ACS Appl. Energy Mater. 5 (2022) 575–584, https://doi.org/10.1021/acsaem.1c03094.
[80] G. Kresse, J. Hafner, Ab initio molecular dynamics for open-shell transition metals, Phys. Rev. B 48 (1993) 13115–13118, https://doi.org/10.1103/physrevb.48.13115.
[81] G. Kresse, J. Furthmüller, Efficient iterative schemes for ab initio total-energy calculations using a plane-wave basis set, Phys. Rev. B 54 (1996) 11169, https://doi.org/10.1103/PhysRevB.54.11169.
[82] G. Kresse, J. Furthmüller, Efficiency of ab-initio total energy calculations for metals and semiconductors using a plane-wave basis set, Comput. Mater. Sci. 1 (1996) 15–50, https://doi.org/10.1016/0927-0256(96)00008-0.
[83] J.P. Perdew, K. Burke, M. Ernzerhof, Generalized gradient approximation made simple, Phys. Rev. Lett. 77 (1996) 3865, https://doi.org/10.1103/PhysRevLett.78.1396.
[84] P.E. Blöchl, Projector augmented-wave method, Phys. Rev. B 50 (1994) 17953, https://doi.org/10.1103/PhysRevB.50.17953.
[85] E. Olsson, X. Aparicio-Anglès, N.H. De Leeuw, A computational study of the electronic properties, ionic conduction, and thermal expansion of $Sm_{1-x}A_xCoO_3$ and $Sm_{1-x}A_xCoO_{3-x/2}$ (A = Ba^{2+}, Ca^{2+}, Sr^{2+}, and x = 0.25, 0.5) as intermediate temperature SOFC cathodes, J. Chem. Phys. 145 (2016) 14703, https://doi.org/10.1039/c7cp01555k.